DOI: 10.1016/j.jmmm.2022.169409

Journal of Magnetism and Magnetic Materials 556 (2022) 169409

Contents lists available at ScienceDirect

Journal of Magnetism and Magnetic Materials

journal homepage: www.elsevier.com/locate/jmmm

Resolving magnetic contributions in $BiFeO_3$ nanoparticles using First order reversal curves

A. Cardona-Rodríguez [a,*], Edwin Ramos Rodríguez [b], D. Carranza-Celis [a], N. Vergara-Duran [a], A.S.E. da Cruz [c], O. Moscoso Londoño [d], F. Béron [c], M. Knobel [c], A. Reiber [e], Diego Muraca [c], Juan Gabriel Ramírez [a]

[a] *Department of Physics, Universidad de los Andes, Bogotá 111711, Colombia*
[b] *Departamento de Ciencias Básicas, Universidad Manuela Beltrán, Bogotá 251046, Colombia*
[c] *Instituto de Física 'Gleb Wataghin', Universidade Estadual de Campinas (UNICAMP), 13083- 859 Campinas, São Paulo, Brazil*
[d] *Departamento de Física y Matemáticas, Universidad Autónoma de Manizales, Manizales 170002, Colombia*
[e] *Department of Chemistry, Universidad de los Andes, Bogotá 111711, Colombia*

A R T I C L E I N F O

Keywords:
Magnetic nanoparticles
Multiferroics
Bismuth Ferrite

A B S T R A C T

$BiFeO_3$ (BFO) nanoparticles (NPs) were studied using First-Order Reversal Curve (FORC) and temperature-dependent magnetometry measurements. The BFO NPs were fabricated by a sol–gel method, while the crystal structure and the average particle radius were obtained by powder X-ray diffraction analysis and Small-Angle X-Ray Scattering (SAXS) measurements, respectively. The NP size varies below and above the typical bulk BFO spin cycloid length ($\lambda = 62$ nm). Below λ, the NPs show ferromagnetic-like hysteresis loops where the saturation magnetization decreases while nanoparticle size rises. This magnetic behavior changes for NP size over λ, which only exhibits a paramagnetic contribution. The FORC distributions indicate the presence of two competing size-dependent contributions to the observed magnetic signal Also, the FORC distributions show that in the ferromagnetic regime there are two competing size-dependent contributions to the observed magnetic signal. Our results suggest the existence of a magnetic core–shell structure in NPs below λ, possibly driven by the strong spin–lattice coupling.

1. Introduction

BFO ($BiFeO_3$) is a remarkable multifunctional material, which exhibits simultaneous ferroelectric and antiferromagnetic behaviors [1]. Bulk BFO is a multiferroic material with Néel temperature $T_N = 643$ K and ferroelectric Curie temperature $T_C = 1143$ K. BFO has attracted great attention due to its potential application in nonvolatile memories, sensors, and nanogenerators [2–4]. Its magnetic structure is G-type antiferromagnetic with a spin cycloid wavelength λ of 62 nm [5,6] which is caused by the Dzyaloshinskii–Moriya anisotropy along the [1 1 0] direction being perpendicular to the polarization axis of the crystal [7]. Recent reports have shown that the magnetic properties can be modified in nanoparticulate and thin-film systems with thickness and size comparable to the cycloidal period length [5,6,8] where the antiferromagnetic behavior can be tuned to like- ferromagnetic when is modified the nanoparticle size, due to the uncompensated spin cycloid in BFO, thus giving rise to multiple magnetic interactions between the surface and the bulk atoms [9].

One way to deconvolute the magnetic contributions from complex and inhomogeneous samples is to study the irreversibility of their magnetic switching mechanisms [10]. This can be done by measuring the First Order Reversal Curves (FORCs) [11–14]. This method can separate the magnetic contributions in systems such as in hybrid ones with hard and soft magnetic mixtures [15] or in magnetic nanostructures with core–shell magnetic structures [16].

In this paper, we report the magnetic contributions to the total magnetization of BFO nanoparticles (NPs) with varying sizes. They present a ferromagnetic behavior up to a size close to the length of the spin cycloid, with a decreasing saturation magnetization as the nanoparticles enlarge, while larger nanoparticles exhibit a paramagnetic behavior similar to other reports for BFO [5,17]. The analysis of zero-field-cooled and field-cooled (ZFC-FC) measurements yields two

---

* Corresponding author.
E-mail address: a.cardona411@uniandes.edu.co (A. Cardona-Rodríguez).

https://doi.org/10.1016/j.jmmm.2022.169409
Received 23 November 2021; Received in revised form 29 March 2022; Accepted 20 April 2022

blocking temperatures in BFO NPs with a radius of 8, 28, and 44 nm. The FORC data agree with the ZFC-FC results. Furthermore, they show a strong dependence on the BFO nanoparticle size, suggesting that the magnetization can be size tuned.

The BFO NPs were prepared by the sol–gel method [18]. The xerogel powder was calcinated at temperatures T_{cal} between 425 °C to 600 °C for 2 h to obtain NPs of different sizes. Their X-ray diffraction (XRD) data were measured on a PANalyticalX'Pert Pro MDP and a PANalytical Empyrean setups, using the Bragg–Brentano geometry with a CuK_{α} radiation and an angular step size of 0.01°. The small-angle X-ray scattering (SAXS) measurements were performed on a Malvern Panalytical Empyrean equipment. The EasySaxs software was used to analyze the SAXS data and to determine the particle size distribution [19] of the samples with a T_{cal} from 425 to 550 °C[1].

The magnetic characterizations were performed in a vibrating sample magnetometer (VSM) Lake Shore 7400 at room temperature and in a Quantum Design™ SQUID magnetometer. The isothermal hysteresis loops were acquired sweeping the magnetic field from −1.2 T to 1.2 T at room temperature. The magnetization (M) behavior as a function of temperature (T) was obtained under zero-field-cooling (ZFC) and field-cooling (FC) protocols in a temperature range from 5 to 300 K, with an external magnetic field of 0.01 T. The blocking temperature distribution $f(T_B)$, and hence its mean value $\langle T_B \rangle$, can be extracted through the derivative with respect to the temperature of the difference between the zero-field-cooling magnetization (M_{ZFC}) and field-cooling magnetization (M_{FC}) curves [20], i.e. $f(T_B) = d(M_{ZFC} - M_{FC})/dT$.

The FORC experiments were done in a VSM system, by measuring the reversal curves at room temperature by increasing the magnetic field up to a saturation field $H_s = 0.3$ T, then decreasing the field to a reversal field H_r, followed by an increase of the field back to $H_s = 0.3\mathrm{T}$ with a field step of $H_{step} = 2.4161$ mT until completing the path from H_s down to $-H_s$. The averaging time per point was kept fixed at 0.5 s. To improve the signal-to-noise ratio, we performed an average of up to three FORC sets, to finally obtain a FORC distribution called $\mathrm{FORC}_{\mathrm{ave}}$.

The FORC distribution is defined as [12]:

$$\rho(H_r, H_b) = -\frac{1}{2}\frac{\partial^2 M(H_r, H_b)}{\partial H_r \partial H_b}, \tag{1}$$

being H_{r} is the reversal field and H_{b} the applied field. Usually, $\rho(H_{\mathrm{r}}, H_{\mathrm{b}})$ is plotted using the transformations $H_c = (H_b - H_r)/2$ and $H_u = (H_b + H_r)/2$. In the classical Preisach model, the H_u axis corresponds to the distribution of local interaction fields, while the H_c one to the distribution of switching fields. From here, one can obtain the average coercivity related to the distributions H_{c} that are associated with the existence of different domains and magnetic reversal mechanisms [10,14,21,22].

The FORC distribution can be effectively decomposed using the central ridge distribution, for quantitative analysis, the central ridge (ρ_{CR}) can be separated from other contributions. The method of separation is based on extrapolation of the regular part of the FORC distribution (ρ) under the region occupied by (ρ_{CR}). The ridge can be described as $\rho_{CR} = \frac{1}{2} f_{CR}(H_c)\delta(H_b)$, where f_{CR} is the central ridge coercivity contributions (ρ_{CR} is regularized by the Dirac distribution with an appropriate function of H_b). The central ridge coercivity distribution is obtained in two steps: first, the central ridge contribution ρ_{CR} to the FORC diagram is isolated from continuous background, second, ρ_{CR} is integrated over H_b. While the amplitude of ρ_{CR} depends on the resolution of measurements FORC, f_{CR} is independent of any measuring and processing parameter and shows properties intrinsic magnetic properties H_b [22] which is calculated by replacing $f_{CR} = \rho(H_c, H_u = 0)$, centered along the H_c axis. The function f_{CR} might be called a coercivity distribution [22]. To isolate the interaction and single reversal signals from the FORC distributions, we extracted the central ridge from the $\mathrm{FORC}_{\mathrm{ave}}$ distributions following the protocol presented by R. Egli [12,23] for each T_{cal} value.

Both the backfield coercivity and reversal coercivity distribution [12] can also be extracted from the FORC measurements. The backfield coercivity is obtained for a saturated sample by measuring the remanent magnetization after the application of large negative magnetic fields (the applied negative fields being equivalent to reversal fields H_r). The backfield demagnetization curve is calculated using:

$$f_{bf}(H_r, H_b) = -\frac{1}{2}\frac{\partial M(H_r, 0)}{\partial H_r}\bigg|_{Hr=H} \tag{2}$$

Similarly, the irreversal coercivity distribution (f_{irr}) used to calculate irreversible magnetization changes, f_{irr} is defined in analogy with the backfield coercivity distribution as:

$$f_{irr}(H_r, H_b) = -\frac{1}{2}\frac{\partial M(H_r, H)}{\partial H_r}\bigg|_{Hr=H} \tag{3}$$

2. Results

The Rietveld refinement of all sample XRD measurements confirms that most reflections coincide with the Bragg planes expected for a BFO crystal with R3c space group of symmetry with a χ^2 less than 10 (see Fig. S1 and Table S1 in supplemental materials). Only a low percentage (in total less than 10%) of secondary phases were found. From the SAXS measurements, we achieved to determine the nanoparticle average radius ($\mathrm{R}_{\mathrm{ave}}$) and surface to volume ratio (Fig. S2 and Table 1).

Fig. 1 shows the isothermal magnetization hysteresis loops (M versus H) measured at room temperature. Notice that for the samples calcinated at temperatures between 425 and 550 °C, it is possible to observe a characteristic S-shape curve with a low remanence and an almost null coercivity (see Fig. 1a for a low magnetic field zoom). The M vs. H data suggest a weak ferromagnetic-like behavior for these NPs. However, the sample with $T_{\mathrm{cal}} = 600$ °C presents a paramagnetic behavior with a lower magnetic moment than in those systems T_{cal} (See Fig. 1b). This small paramagnetic signal is similar to those observed in the previous reports [5,17]. The magnetization of the BFO NPs in this study is considerably larger than in other ones, where sol–gel methods are used [5,17], since the BFO properties are highly dependent on the growth process [18]. In Fig. 1c, we plot the extracted saturation magnetization M_S as a function of surface to volume ratio (δ). By performing a linear fitting (red line), the intercept with the bottom axis would indicate the δ value needed to reach a null M_S. In our case, it coincides with a value of δ $\approx 0.05\ \mathrm{nm}^{-1}$, which approximately corresponds to an average radius of 60 nm (assuming spherical particles).

Fig. 2a shows the ZFC and FC curves recorded with an external field $H = 0.01$ T, for samples calcinated at 425, 500, and 550 °C. The blocking temperature (T_B) is associated with a transition to the so-called superparamagnetic relaxation process [5]. Considering the size distribution, the distribution of blocking temperatures $f(T_B)$, is also expected. Such distribution can be estimated by subtracting the ZFC and FC branches and calculating the derivative with respect to the temperature, the reached maximum in $f(T_B)$ is associated with the blocking temperature.

Table 1
Average radius ($\mathrm{R}_{\mathrm{ave}}$) and surface-volume ratio (δ) for samples calcinated at different T_{cal}.

$\mathrm{T}_{\mathrm{cal}}$(°C)	425	450	475	500	550
$\mathrm{R}_{\mathrm{ave}}$(nm)	8 ± 5	18 ± 6	24 ± 6	28 ± 5	43 ± 5
δ(nm^{-1})	0.50	0.19	0.13	0.11	0.08

---

[1] For bigger NPs, for example the sample with a Tcal =600 °C, the characterization must be done performed by Ultra Small-Angle X-ray Scattering (USAXS). This experimental technique is used in samples with several hundreds of nanometers. However, our research is focus in nanoparticles with size less to spin cycloidal of BFO (62 nm).

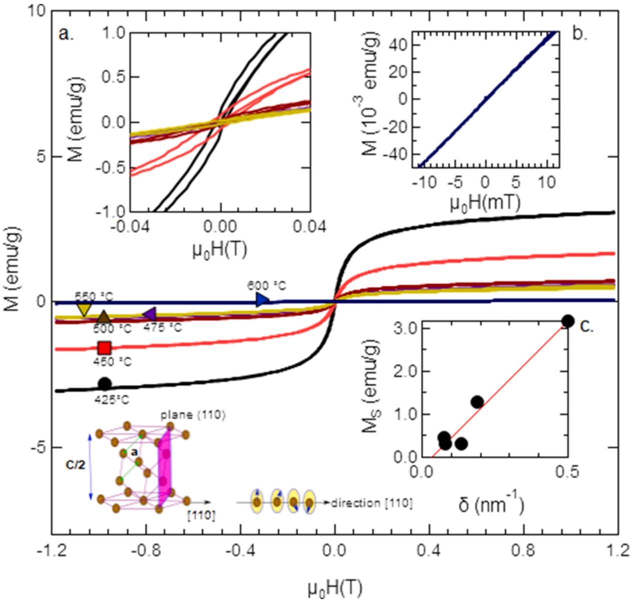

Fig. 1. Room temperature magnetization curves as a function of the magnetic field for BFO NPs synthesized from 425 °C to 600 °C. Inset a. Zoom of the magnetization curves for BFO NPs synthesized from 425 °C to 550 °C. The samples synthesized with a temperature below 550 °C show a weak coercive field. Inset b. Magnetization curve of BFO NPs synthesized at 600 °C, showing a linear behavior. Inset c. shows the calculated saturation magnetization vs.δ for all NPs. The line represents a linear fit. The intercept with the bottom axis corresponds to $\delta = 0.05$ nm^{-1}, which corresponds to a particle with approximately 60 nm radius. Inset show the magnetic cell for BFO in hexagonal representation and the propagation direction of the spin cycloid for BFO.

Fig. 2b presents the obtained $f(T_B)$ for each sample. Notice that $f(T_B)$ can be well fitted using two lognormal-type functions with two different T_B values. The fit results are shown in Fig. 3(c-d), where the mean blocking temperatures associated with each characteristic size are labeled as T_{B1} and T_{B2}, respectively. When the nanoparticle size reduced below λ, the number of decompensated spins on the surface increases with relation to spins the core [8]. Therefore, we can expect that the lower temperature blocked-unblocked transition (T_{B1}) could be more linked to the surface coupled magnetic moments since the related volume is smaller than the nanoparticle core. Excluding morphology effects and other interactions, the Néel-Arrhenius equation for magnetic nanoparticles becomes $T_{B2} = K_V V/25k_B$, where the particle volume is V (in the present case the core volume), the volumetric magnetic anisotropy is K_V and the Boltzmann constant is k_B. This parameter can be useful for a qualitative analysis of our samples [24]. We might expect, by analogy, that surface effects can be correlated with another transition temperature $T_{B1} \propto K_s S/25k_B$, where S is the particle surface area, and the surface magnetic anisotropy is K_S. From the ratio between the two equations, we can obtain $K_s/K_V = T_{B1}/(T_{B2}\delta)$ where the surface to volume ratio is δ. For the samples with T_{cal} of 425, 500, and 550 °C, it gives K_s/K_V values of 0.56, 4.31, and 4.20, respectively. Therefore, the surface anisotropy overcomes the volume for NP radius greater than 28 nm (56 nm of diameter, see supplemental material Fig. S4). This system is not a conventional ferromagnetic system due to the BFO could present uncompensated spins at the core volume and surface. In the low-temperature region (see Fig. 2b), it appears that there are two contributions to the magnetic behavior, as indicated by the two distinct blocking temperatures. However, these two contributions cannot be directly observed by conventional isothermal hysteresis loops. We carried out FORC measurements to map the magnetic interactions that give rise to the isothermal hysteresis loops. The FORC technique is an alternative way to separate distinct magnetic contributions. Fig. 3 shows the corresponding FORC curves (Fig. 3a, d, and g) and the corresponding FORC diagrams (Fig. 3b, e, and h) for the NPs synthesized at 425, 475, and 550 °C. The FORC diagrams were measured in a field range of -200 to 200 mT and the FORC$_{\mathrm{ave}}$ corresponds to the averaged FORCs. It is worth noting that at room temperature, the samples are in the unblocked regime, as suggested by the coercivity in the M vs H measurements (Fig. 1b) and by the separation between the ZFC-FC curves at 300 K (see Fig. 2). We extracted the central ridge FORC$_{\mathrm{ave}}$ distributions (Fig. 3c, f, and i). The Fig. 3c exhibits a single maximum or peak, with an intensity close to 150 emu/Tg at $H_c = 2$ mT along $H_u = 0$ ($T_{\mathrm{cal}} = 425$ °C). The peak position field is called the nucleation field and corresponds to a single reversal mechanism. At $T_{\mathrm{cal}} = 475$ °C (Fig. 3f), two nucleation fields develop (peak 1 and peak2), which persists for higher T_{cal} NPs until the sample with $T_{\mathrm{cal}} = 550$ °C (Fig. 3i). We hypothesize that the first peak (lowest H_c) in each FORC$_{\mathrm{ave}}$ may be related to the ferromagnetic-like contribution of our NPs due to the small coercive field values obtained. The peak close to the origin of the diagram corresponds to grains with superparamagnetic behavior due to a low coercivity [16,25].The second nucleation field centered in $H_u = 0$ around of $H_c = 20mT$, could be related to a system containing SD non-

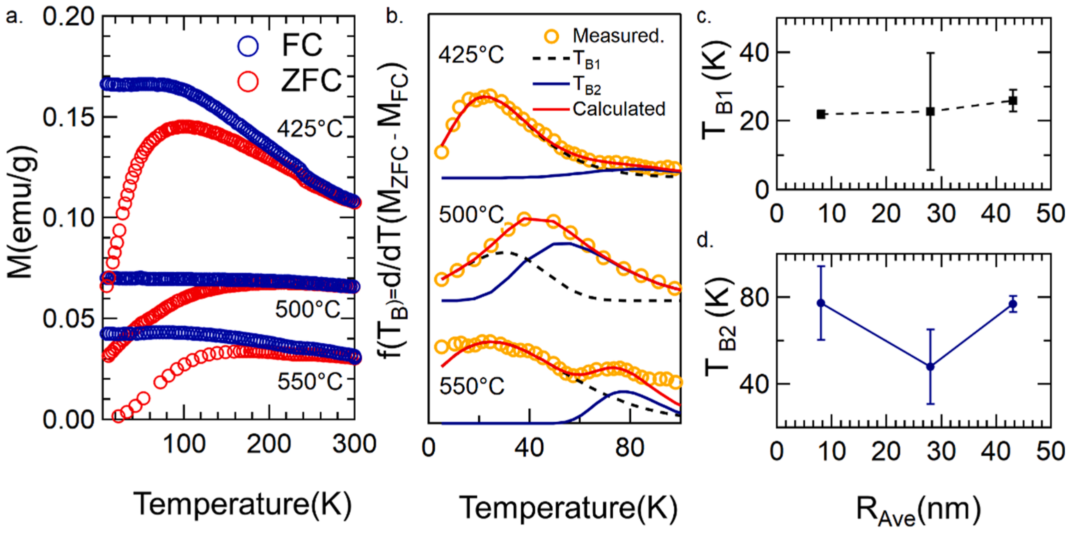

Fig. 2. a. ZFC-FC magnetization curves for BFO NPs calcinated at different calcination temperatures measured under a magnetic field of $H = 0.01$ T. b. Blocking temperature distribution $f(T_B)$, calculated from a), where the lognormal fittings of two contributions are indicated. (c-d) Mean blocking temperatures T_{B1} and T_{B2} as a function of the calcination temperature for each distribution.

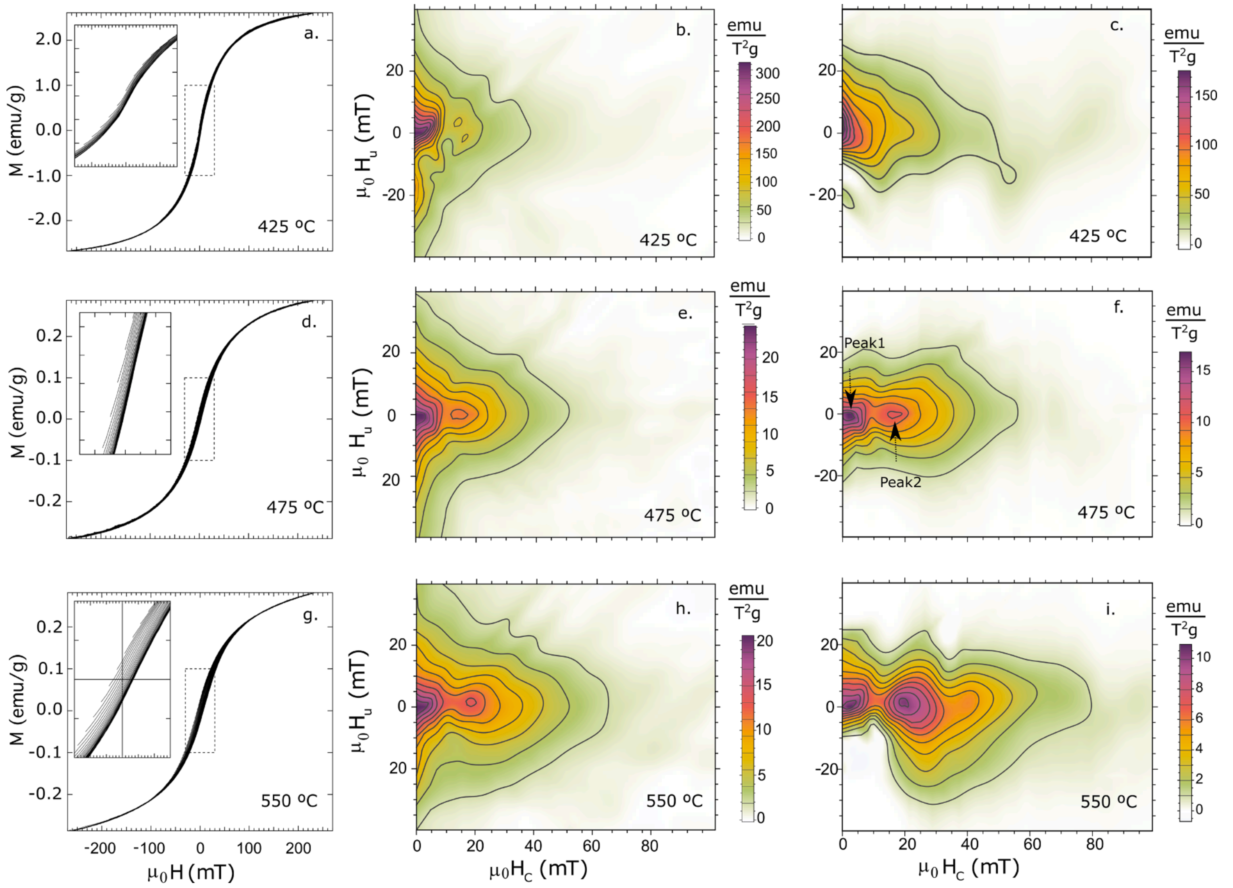

Fig. 3. Room temperature First order reversal curves for BFO NPs synthesized at a. 425 °C, d. 475 °C, and g. 550 °C. Corresponding FORC$_{ave}$ diagrams for BFO NPs b, e, and h. Central ridge distribution (ρ_{CR}) from FORC$_{ave}$ diagrams c, f, and i. The arrows used in the figure f. show the two principal contribution in ρ_{CR}. Note that the color scale is different for each FORC$_{ave}$ diagram. The Figure for the samples with a 450 and 500 are shown in the supplemental material (Fig. S5).

interacting particles [16,22].

To understand these two contributions, we analyzed the central ridge, backfield coercivity, and reversal coercivity distribution. These three coercivity distributions can be seen in Fig. 4 for the samples with T$_{cal}$ at 425, 475, and 550 °C (results for T$_{cal}$ = 450 and 500 °C are shown in the supplemental material, Fig. S6) all coercivity distributions present similar intensities, which is typical for non-interacting particle systems. It can be noticed that the sample synthesized at 425 °C presents a higher irreversible contribution intensity compared to those synthesized at 475 and 550 °C.

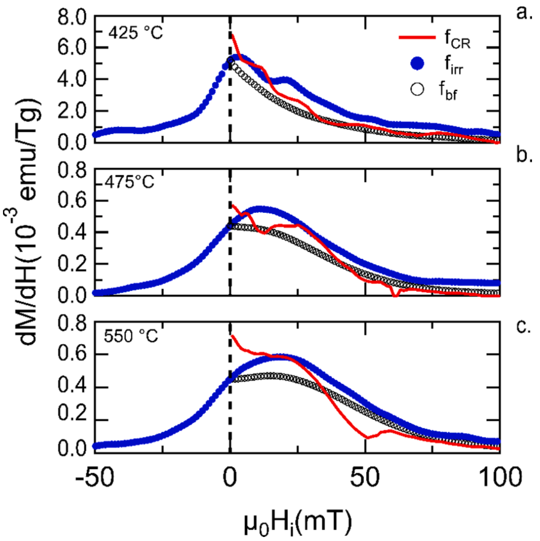

Fig. 4. Coercivity distribution obtained from FORC protocol for the samples with T$_{cal}$ at a. 425 °C, b. 475 °C, c. 550 °C. All coercivity distributions have similar intensity values.

We analyzed those results by separating the coercivity distributions. Fig. 5 (a,b) shows the results for samples with T_{cal} = 425 °C and 500 °C, respectively f_{CR} corresponds to the symbols, while the area depicts its uncertainty (See Fig. S5 for the full set of measurements). We fitted the f_{CR} curve assuming Gaussian distribution functions centered at the nucleation fields, from which we extracted the main two contributions (D$_1$ and D$_2$), that correspond to more than 70 % of the total signal. These two contributions correspond to the two peaks seen in the FORC$_{ave}$ diagrams in Fig. 2. We believe that D$_1$, being close to zero coercivity, should account for superparamagnetic contributions and D$_2$, should represent a single-domain reversal contribution typical of a ferromagnetic-like material.

For the T_{cal} = 425 °C sample, it appears that two nucleation fields are present (similar results can be found for the reversal coercivity and backfield distributions, see Fig. S8 and Fig. S9), one labeled D$_2$, centered around 8 mT, and another one D$_1$. Fig. 5b shows ρ_{CR} for the T_{cal} = 500 °C sample. The two switching field contributions are more distinct, one around 5 mT, and the second one around 18 mT. In both cases, we plotted the individual contributions indicated by the labels D$_1$ and D$_2$. The results from the fitting procedure of all FORC$_{ave}$ distributions are presented in Fig. 5c-d. In Fig. 5c the peak areas give information about the number of domains with similar nucleation fields (note the semi-log scale). Interestingly, both contributions follow the same trend: when the radius is bigger than 28 nm (56 nm diameter), the area in each

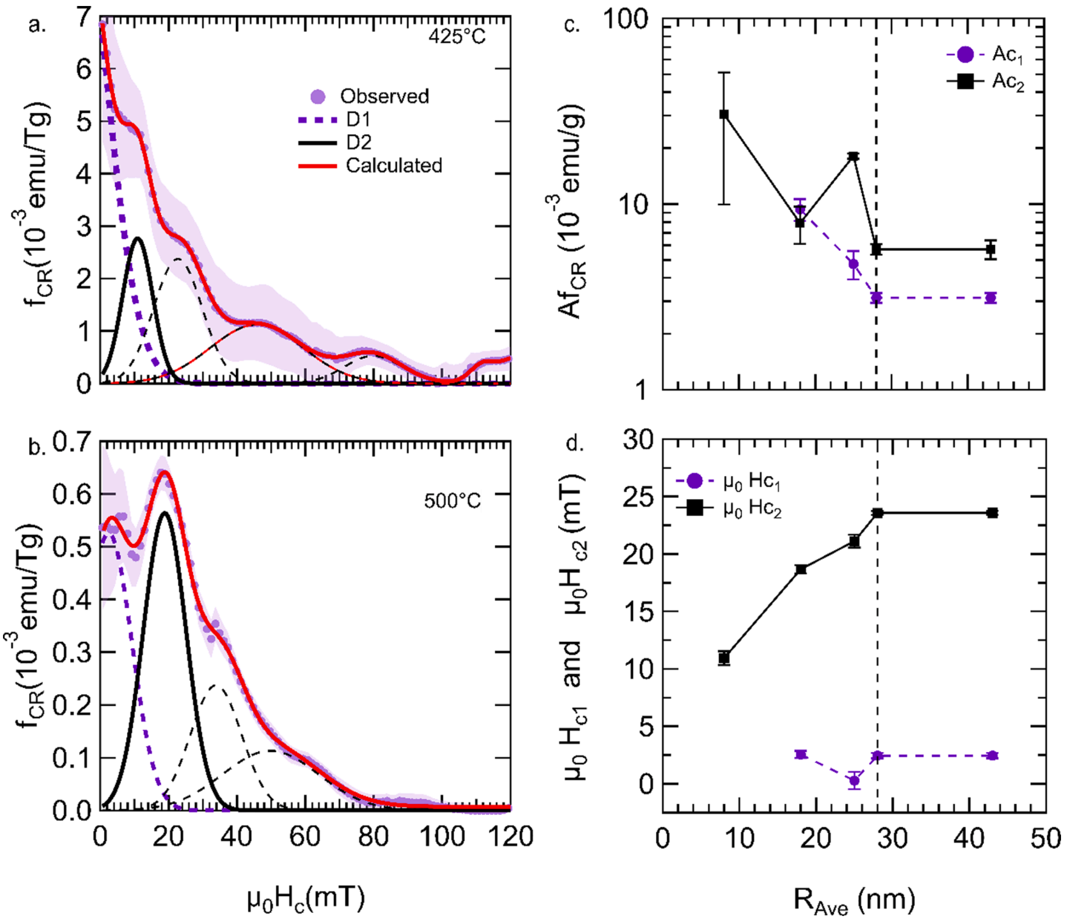

Fig. 5. a. ρ_{CR} distribution as a function of H_C (symbols) as obtained from the $FORC_{ave}$ for the sample with $T_{cal} = 425$ °C (8 nm). The highlighted region corresponds to the fitting model uncertainty. Dash lines correspond to the main contribution of the ρ_{CR} distributions D_1 and D_2. The fitting model is represented by the red solid line. Similarly, in b. the fitting for the sample grown at $T_{cal} = 500$ °C (28 nm) is showed. c. Areas of the corresponding D_1 and D_2 contributions (A_1 and A_2) obtained for all sample sets. d. Coercive fields extracted from ρ_{CR} as a function of the particle size. The vertical dashed lines in c. and d. are a guide to the eye centered at R_{ave} = 28 nm.

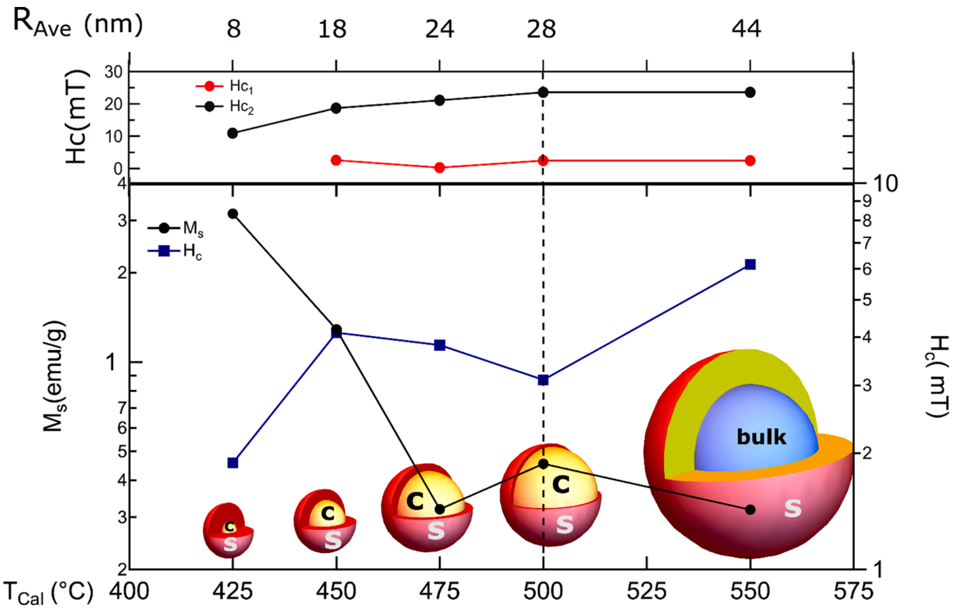

Fig. 6. M_S and H_C obtained from Fig. 2a as a function of particle radius and calcination temperature, also H_{C1} and H_{C2} are presented in the upper figure obtained of central ridge results. The sketch depicts the evolution of the core–shell (C-S) particle structure as deduced by the FORC measurements. The bulk region refers to an area inside the particle that is magnetically compensated (antiferromagnetic). The red and yellow regions are magnetically uncompensated and thus ferromagnetic-like. The vertical dashed line is a guide to the eye centered at R_{ave} = 28 nm.

distribution decrease with an increasing average radius. Similarly, the nucleation field values follow an increasing trend with particle radius. Both contributions present a trend modification at a size indicated by the vertical dotted line. Interestingly, this behavior points to a critical BFO size, where the intensity in the central ridge is increased. This size nanoparticle is close to the BFO-bulk value of the spin cycloid. This trend is similar to the area contribution, as shown in Fig. 5c. In all cases, the sample with 56 nm diameter shows a signature of change in the trend. These results indicate a deep correlation between the particle size and their overall magnetism. Fig. 6 depicts such a scenario using the superposition of the M_S and H_C plots for each case, extracted from dc magnetic measurements in Fig. 2a. The magnetic moment decreases with increasing particle size probably due to an increase in the compensated spins. Reaching the size above the spin cycloid length, the particle core is magnetically compensated, and probably antiferromagnetically aligned as expected for bulk BFO. The BFO excess beyond the spin cycloid length is then ferromagnetically uncompensated at the surface. At this stage, the magnetic signal would be minimal since the surface-to-volume ratio decreases considerably, and the overall signal is dominated by the entire volume. This could explain the significant reduction in the saturation magnetization, even reaching a paramagnetic signal (see Fig. 2c). Fig. 6 shows the H_{c1} and H_{c2} obtained from the central ridge analysis, H_{c1} and H_{c2} values could show as change the coercivities at the core and shell in BFO NPs.

From our experimental results, one can conclude that two main contributions to the magnetic properties coexist in our samples and that there is a critical size at which the irreversible process stabilizes. Interestingly, from the FORC distributions, we see that this critical size coincides with particles of $R_{\text{ave}} = 28$ nm, which is close to the spin cycloid length in BFO bulk. On the other hand, the two main contributions to the BFO magnetism can be associated with a core–shell structure [9,16]. Both contributions must be ferromagnetic-like, probably due to uncompensated spins along the spin cycloid, the spins are uncompensated in the core and shell of the BFO NPs, when the nanoparticle size decreases, the number of atoms at the surface increases with relation to the number of atoms in the core. The superparamagnetic contribution is present in all the samples. We take as the hypothesis that the superparamagnetic contribution could be associated with the shell, when it is reduced the nanoparticle size, the superparamagnetic contribution is increasing. This trend can be seen in the FORC diagrams (see Fig. 3 c, f, and i) and corroborated by the ZFC-FC curves (see Fig. 2a). In addition to this, we built a 3D Ising model of a core–shell particle array to calculate their FORC distributions. We found that is possible to distinguish the two magnetic contributions of the core–shell array (see Fig. S10a-f). These results support the use of the FORC method to distinguish ferromagnetic-like contributions.

We can conclude that there must be a magnetic inhomogeneity in our BFO NPs that accounts for the evidence of two well-defined magnetic signatures as obtained by FORC and ZFC-FC measurements. The most plausible explanation, as previously suggested [9], is the existence of an intrinsic magnetic core–shell structure. For BFO nanoparticles, the core shell (C-S) is ferromagnetic-like, due to the uncompensated spin cycloid. The fact that the surface is magnetically different might come from the larger number of atoms at the surface giving different values of magnetic anisotropy for the core, K_V, and shell K_s, as shown by ZFC-FC measurements (Fig. 2).

In summary, we successfully synthesized BFO nanoparticles. The structural characterization shows NPs with a distorted rhombohedral crystal lattice, while magnetization measurements at room temperature show that the magnetic behavior can be tuned from antiferromagnetic to weak ferromagnetic behaviors by controlling the nanoparticle size. By using the FORC approach, we deconvoluted the magnetic contributions in the NPs. According to the overall behavior of the individual coercivity distribution intensities, we consider that both contributions have a different origin that may be related to a core–shell structure. This is supported by magnetometry and FORC measurements. Consequently, our results point to an intrinsic core–shell structure that is formed in BFO NPs with size near to a spin cycloid length. Our results shed light on future spintronics devices exploiting the additional degrees of freedom induced in BFO by controlling their size at the nanoscale.

Declaration of Competing Interest

The authors declare that they have no known competing financial interests or personal relationships that could have appeared to influence the work reported in this paper.

Acknowledgments

We acknowledge support from Facultad de Ciencias and Vicerrectoria de Investigaciones of Universidad de los Andes, Bogotá, Colombia. A.C.R acknowledges financial supportfrom proyectos semilla-Facultad de Ciencias at Universidad de los Andes (2019-II). E.R acknowledges Colciencias-Colfuturo Universidad Nacional de Colombia for its support under “convocatoria 617- Doctorados Nacionales”. MK, A. S.E.C and FB acknowledge the support from Brazilian agencies Fundação de Amparo à Pesquisa do Estado de São Paulo (FAPESP) (projects #2017/10581-1 and #2020/07397-7) and Conselho Nacional de Desenvolvimento Científico e Tecnológico (CNPq) –Finance code 001 and projects 436573/2018-0 and #312762/2021-6.

Appendix A. Supplementary material

Supplementary data to this article can be found online at https://doi.org/10.1016/j.jmmm.2022.169409.

Reference

[1] N.A. Spaldin, S.W. Cheong, R. Ramesh, Multiferroics: Past, present, and future, Phys. Today. 63 (2010) 38–43, https://doi.org/10.1063/1.3502547.

[2] R. Sankar Ganesh, S.K. Sharma, S. Sankar, B. Divyapriya, E. Durgadevi, P. Raji, S. Ponnusamy, C. Muthamizhchelvan, Y. Hayakawa, D.Y. Kim, Microstructure, structural, optical and piezoelectric properties of $BiFeO_3$ nanopowder synthesized from sol-gel, Curr. Appl. Phys. 17 (2017) 409–416, https://doi.org/10.1016/j.cap.2016.12.008.

[3] A. Cardona Rodríguez, I.C. Arango, M.F. Gomez, C. Dominguez, J. Trastoy, C. Urban, S. Sulekar, J.C. Nino, I.K. Schuller, M.E. Gomez, J.G. Ramírez, Resistive switching in multiferroic $BiFeO_3$ films: Ferroelectricity versus vacancy migration, Solid State Commun. 288 (2019) 38–42, https://doi.org/10.1016/j.ssc.2018.11.005.

[4] S. Chakraborty, M. Pal, Highly efficient novel carbon monoxide gas sensor based on bismuth ferrite nanoparticles for environmental monitoring, New J. Chem. 42 (2018) 7188–7196, https://doi.org/10.1039/c8nj01237g.

[5] F. Huang, Z. Wang, X. Lu, J. Zhang, K. Min, W. Lin, R. Ti, T. Xu, J. He, C. Yue, J. Zhu, Peculiar magnetism of $BiFeO_3$ nanoparticles with size approaching the period of the spiral spin structure, Sci. Rep. 3 (2013) 2907, https://doi.org/10.1038/srep02907.

[6] D. Carranza-Celis, A. Cardona-Rodríguez, J. Narváez, O. Moscoso-Londono, D. Muraca, M. Knobel, N. Ornelas-Soto, A. Reiber, J.G. Ramírez, Control of Multiferroic properties in $BiFeO_3$ nanoparticles, Sci. Rep. 9 (2019) 3182, https://doi.org/10.1038/s41598-019-39517-3.

[7] W. Ratcliff, D. Kan, W. Chen, S. Watson, S. Chi, R. Erwin, G.J. McIntyre, S. C. Capelli, I. Takeuchi, Neutron diffraction investigations of magnetism in BiFeO3 epitaxial films, Adv. Funct. Mater. 21 (9) (2011) 1567–1574.

[8] T.J. Park, G.C. Papaefthymiou, A.J. Viescas, A.R. Moodenbaugh, S.S. Wong, Size-dependent magnetic properties of single-crystalline multiferroic $BiFeO_3$ nanoparticles, Nano Lett. 7 (2007) 766–772, https://doi.org/10.1021/nl063039w.

[9] F. Huang, X. Xu, X. Lu, M. Zhou, H. Sang, J. Zhu, The exchange bias behavior of $BiFeO_3$ nanoparticles with natural core-shell structure, Sci. Rep. 8 (2018) 2311, https://doi.org/10.1038/s41598-018-19676-5.

[10] A.P. Roberts, D. Heslop, X. Zhao, C.R. Pike, Understanding fine magnetic particle systems through use of first-order reversal curve diagrams, Rev. Geophys. 52 (2014) 557–602, https://doi.org/10.1002/2014RG000462.

[11] C.R. Pike, A.P. Roberts, K.L. Verosub, Characterizing interactions in fine magnetic particle systems using first order reversal curves, J. Appl. Phys. 85 (1999) 6660–6667, https://doi.org/10.1063/1.370176.

[12] R. Egli, VARIFORC: An optimized protocol for calculating non-regular first-order reversal curve (FORC) diagrams, Glob. Planet. Change. 110 (2013) 302–320, https://doi.org/10.1016/j.gloplacha.2013.08.003.

[13] R. Pike, First-order reversal-curve diagrams and reversible magnetization, Phys. Rev. B. 68 (2003), 104424, https://doi.org/10.1103/PhysRevB.68.104424.

[14] M. Kumari, M. Widdrat, É. Tompa, R. Uebe, D. Schüler, M. Pósfai, D. Faivre, A. M. Hirt, Distinguishing magnetic particle size of iron oxide nanoparticles with first-order reversal curves, J. Appl. Phys. 116 (2014) 124304, https://doi.org/10.1063/1.4896481.

[15] D.R. Cornejo, T.R.F. Peixoto, S. Reboh, P.F.P. Fichtner, V.C. de Franco, V. Villas-Boas, F.P. Missell, First-order-reversal-curve analysis of Pr-Fe-B-based exchange spring magnets, J. Mater Sci. 45 (18) (2010) 5077–5083.

[16] A. Juhin, A. López-Ortega, M. Sikora, C. Carvallo, M. Estrader, S. Estradé, F. Peiró, M.D. Baró, P. Sainctavit, P. Glatzel, J. Nogués, Direct evidence for an interdiffused intermediate layer in bi-magnetic core-shell nanoparticles, Nanoscale 6 (2014) 11911–11920, https://doi.org/10.1039/c4nr02886d.

[17] M. Hasan, M.F. Islam, R. Mahbub, M.S. Hossain, M.A. Hakim, A soft chemical route to the synthesis of BiFeO3 nanoparticles with enhanced magnetization, Mater. Res. Bull. 73 (2016) 179–186, https://doi.org/10.1016/j.materresbull.2015.09.007.

[18] X. Bai, M. Bugnet, C. Frontera, P. Gemeiner, J. Guillot, D. Lenoble, I.C. Infante, Crystal Growth Mechanisms of $BiFeO_3$ Nanoparticles, Inorg. Chem. 58 (2019) 11364–11371, https://doi.org/10.1021/acs.inorgchem.9b00461.

[19] J. Bolze, V. Kogan, D. Beckers, M. Fransen, High-performance small- and wide-angle X-ray scattering (SAXS/WAXS) experiments on a multi-functional laboratory goniometer platform with easily exchangeable X-ray modules, Rev. Sci. Instrum. 89 (2018) 085115, https://doi.org/10.1063/1.5041949.

[20] M. Knobel, W.C. Nunes, L.M. Socolovsky, E. De Biasi, J.M. Vargas, J.C. Denardin, Superparamagnetism and other magnetic features in granular materials: A review on ideal and real systems, J. Nanosci. Nanotechnol. 8 (2008) 2836–2857, https://doi.org/10.1166/jnn.2008.15348.

[21] A.M. Hirt, G.A. Sotiriou, P.R. Kidambi, A. Teleki, Effect of size, composition, and morphology on magnetic performance: First-order reversal curves evaluation of iron oxide nanoparticles, J. Appl. Phys. 115 (2014) 044314, https://doi.org/10.1063/1.4863543.

[22] R. Egli, A.P. Chen, M. Winklhofer, K.P. Kodama, C.-S. Horng, Detection of noninteracting single domain particles using first-order reversal curve diagrams, Geochem, Geophys. Geosyst. 11 (1) (2010) n/a–n/a.

[23] J. Kind, A.U. Gehring, M. Winklhofer, A.M. Hirt, Combined use of magnetometry and spectroscopy for identifying magnetofossils in sediments, Geochem, Geophys. Geosyst. 12 (8) (2011) n/a–n/a.

[24] T.E. Torres, E. Lima, A. Mayoral, A. Ibarra, C. Marquina, M.R. Ibarra, G.F. Goya, Validity of the Néel-Arrhenius model for highly anisotropic $CoxFe_3$-xO_4 nanoparticles, J. Appl. Phys. 118 (2015) 183902, https://doi.org/10.1063/1.4935146.

[25] C.R. Pike, A.P. Roberts, K.L. Verosub, First-order reversal curve diagrams and thermal relaxation effects in magnetic particles, Geophys. J. Int. 145 (2001) 721–730, https://doi.org/10.1046/j.0956-540X.2001.01419.x.